



## Ni–Mn based alloys as versatile catalyst for different electrochemical reactions

Omar Aaboubi <sup>a,\*</sup>, Ahmed-Yassin Ali-Omar <sup>b</sup>, Eunice Dzoyem <sup>a</sup>, Jimmy Marthe <sup>c</sup>, Mohamed Boudifa <sup>c</sup>

<sup>a</sup> Laboratoire d'Ingénierie et Sciences des Matériaux (LISM), Université de Reims Champagne Ardenne, UFR Sciences, BP1039, 51687 Reims Cedex 2, France

<sup>b</sup> Université de Djibouti, BP 1904, Djibouti

<sup>c</sup> CRITT-MTDS, 08000 Charleville-Mézières, France



### HIGHLIGHTS

- Polarization potential sequence and bath temperature were optimized to produce low cost Ni–Mn catalysts.
- Higher operating bath temperature contributed to produce high active surface deposits.
- The catalysts versatility was tested for various electrochemical reactions.
- Spongy structure and high active surface Ni–Mn catalysts could be obtained at temperature high than 60 °C.

### ARTICLE INFO

#### Article history:

Received 22 January 2014

Received in revised form

3 June 2014

Accepted 25 June 2014

Available online 14 July 2014

#### Keywords:

Nickel–manganese alloys

Catalysts

Hydrogen production

Water electrolysis

Ethanol

Impedance

### ABSTRACT

To develop large scale use of hydrogen and fuel cells as a renewable energy source it is need to increase their durability and reduce their cost mainly due to the use of precious metals. We have examined new type of the low cost binary nickel–manganese (Ni–Mn) catalysts electrodeposited from ammonium chloride bath onto copper substrates. By varying bath composition, polarization potential and essentially bath temperature the operating deposition conditions were optimized to produce Ni–Mn coatings with high active surface (e.g. spongy aspect). The outstanding catalytic activity, the durability and the versatility of the deposited films have been characterized in basic media using several electrochemical processes, such as hydrogen evolution reaction (HER), water oxidation reaction (OER) and ethanol oxidation reaction (EOR).

© 2014 Elsevier B.V. All rights reserved.

### 1. Introduction

As results of the growing energy demand and the energy dependency on fossil fuels which causes serious environmental problems, renewed consideration in the energy sector have significantly revived interest in fuel cells (FCs) and hydrogen energy [1–12]. However, among the obstacles associated with the large-scale commercialization of this technology is limited by the severe dependence of anode and cathode catalyst on a noble and scarce metal, mainly due to the use of precious metals [5]. In the 2008 annual report of DOE, James et al. [7] said that major stack

cost reductions are not currently projected as a result of manufacturing method change or material selection. They conclude that catalyst cost (especially platinum) is the largest single cost contributor, so any efforts to reduce the amount used will yield large savings [7]. However, cost and durability are still the two major barriers for large-scale manufacturing and full commercialization of this technology. The precious metal catalyst is the only fuel cell stack component that will not benefit from economies of scale, and an increase in the demand for fuel cell power systems is bound to drive up the already high price of Pt, about \$1440 per troy ounce at present [8]. Thus, developing high-performance, low-cost, and highly durable catalysts is the number one set of priorities for electrolyzers and FCs research [7,9].

Nickel is one of the most frequently used substrates for practical applications, mainly due to its improved catalytic activity and much

\* Corresponding author.

E-mail address: [omar.aaboubi@univ-reims.fr](mailto:omar.aaboubi@univ-reims.fr) (O. Aaboubi).

lower cost than noble metals. Broad application of nickel and nickel-based alloys coatings results from their special properties such as good corrosive resistance in aggressive environments and high catalytic activity in many electrochemical processes [10–13].

In the last several years a growing attention was paid to the development, synthesis and characterization of Ni–Mn thin films fabricated by electrodeposition method. Ni–Mn alloys are of interest because of their extensive applications as protective coatings, magnetic micro-electro-mechanical systems, or magnetic memory media [14–19]. To the best of our knowledge, only a few publications discussing the use of Ni–Mn alloys as electrocatalyst material in hydrogen production [20–24].

Two properties play an important role in selecting catalytically active materials: (a) the intrinsic activity of the material, which is directly connected to the chemical nature of the materials and (b) the catalyst active surface. Various nickel-based alloys prepared by leaching procedure have been reported to be very effective to increase the active surface catalysts [11,22,25]. In previous work, we have shown that the modifications of active surface by application of external magnetic field during Ni–Mo electrodeposition process leads to catalysts with high performance for HER [12]. In this work, Ni–Mn alloys were deposited and their catalytic properties were tested for hydrogen evolution (HER) water electro-oxidation reaction (OER) and during alcohols electro-oxidation. In order to increase the catalytic performance of the Ni–Mn catalysts, we have performed new deposition conditions to obtain porous electrode without the usual leaching procedure. These investigations are devoted to the applied aspect of this subject. Kinetic studies and fundamental work will be published in forthcoming papers.

## 2. Materials and methods

### 2.1. Cell and electrodes

The deposit preparation was performed in a conventional three-electrode cell using copper disk as working electrode (WE). The Cu substrate was made of Cu pad (diameter  $\varnothing = 11.5$  mm and 5 mm thick) sealed in an epoxy resin thus given available surface area ( $A = 1.04 \text{ cm}^2$ ). The reference electrode was a commercial saturated calomel electrode (SCE) and the counter electrode (CE) was a large surface area nickel rod to minimize the  $\text{Ni}^{2+}$  ions depletion in the solution. For manganese deposition a graphite rod was used as CE. The Cu substrate was mechanically polished first with emery paper (Struers P 1200 & P 4000), then to a mirror on felt with 1  $\mu\text{m}$  alumina and after rinsed with water then with ethanol followed by extensive rinsing with water and dried. The temperature was maintained at controlled value  $T_{\text{bath}} \pm 0.5^\circ\text{C}$  by circulating water in double jacket 100 mL glass beaker. After deposition of catalytic materials, the electrode surface was carefully rinsed with water in order to remove any residual bath chemicals. All measurements were made in natural aeration. The working electrode was maintained in the vertical position under natural convection regime and to facilitate the gas release during experiment. For the study of the catalysts stability, a two-electrode cell was used. In this case, anode and cathode were two identical Ni–Mn catalysts freshly prepared at  $T_{\text{bath}} = 61^\circ\text{C}$ .

### 2.2. Chemicals

Deionized water was used throughout the experiments. Chemical components used in this work were purchased from Prolabo and Fluka and used without further purification. The bath chemical composition of the used solutions is reported in Table 1. The solution pH value was adjusted to  $4.5 \pm 0.1$  by addition of

**Table 1**  
Chemical composition and pH value of baths deposition.

	B1	B2	B3
$\text{NiCl}_2 \cdot 6\text{H}_2\text{O}$	0.105 M	0	0.105 M
$\text{MnCl}_2 \cdot 2\text{H}_2\text{O}$	0	0.155 M	0.155 M
$\text{NH}_4\text{Cl}$	0.935 M	0.935 M	0.935 M
pH	4.5	4.5	4.5

adequate quantities of  $\text{H}_2\text{SO}_4$  or  $\text{NaOH}$  solution. To avoid some pH solution variations, due to hydrogen gas formation during deposition step, solution was renewed after each experiment. In certain case the pH variation may reach up to  $\Delta\text{pH} = 0.5$  after two successive deposition experiments. For kinetic study and catalytic performance characterization 1 M NaOH solutions were used for HER and OER studies. For EOR studies, all solutions were prepared from various quantities of ethanol and 1 M NaOH.

### 2.3. Electrochemical measurements

Cyclic voltammetric (CV), potentiometric and amperometric experiments were performed using Radiometer (PGZ-100) Potentiostat/Galvanostat equipment controlled by VoltaMaster-4 software. The electrochemical impedance spectroscopy (EIS), measurements were carried out using a Potentiostat/Galvanostat (Solartron 1286) and a frequency response analyser (Solartron 1250) monitoring by commercial Software Zplot 2.4 (Scribner Associates). The frequency range examined here lies from 20 kHz to 1 mHz and to get the EIS measurements in the linear mode, a sine wave potential amplitude of  $\Delta E = 10 \text{ mV rms}$  was used.

### 2.4. Physical characterization

In this case the Cu substrate was a flat plaque recovered with an adhesive scotch tape and a circular disk of 11.5 mm diameter was cut to let available Cu exposed portion as WE. For the as-prepared catalyst, the chemical composition and surface morphology was analyzed by high resolution scanning electron microscopy SEM (JEOL JSM 6460LA) coupled with an EDS JEL 1300 microprobe. After oxidation test the surface chemical state of the deposits was characterized using an X-ray diffractometer (D8 advance Bruker) and an ESCALAB 250 spectrometer was used to perform the XPS analysis.

### 2.5. Electrochemically accessible surface area

The electrochemically accessible surface area (ECSA), is an area of a catalyst that is actually available for electrochemical reaction. It may be evaluated from cyclic voltammetry by determining the charge transferred during adsorption of hydrogen on the surface of the platinum catalyst,  $Q_H$ . The ECSA of such electrode may be calculated by using the following relation

$$S_{\text{Pt}} = \frac{Q_H}{250} = \frac{1}{V_b} \int_{250}^{IdE} \frac{IdE}{250} \quad (1)$$

where  $250 \mu\text{C cm}^{-2}$  is the charge transferred during monolayer hydrogen adsorption on a polycrystalline platinum electrode in the assumption that one hydrogen atom is adsorbed on one platinum crystallite [26–30]. Among the different experimental methods used to evaluate the surface of a solid electrode, measuring the mass transfer voltammetry potentiostatic mode has been suggested [26]. According to the Randels–Sevcik relationship, in the case of quiescent solution, the peak current is proportional to the ECSA as following [26]

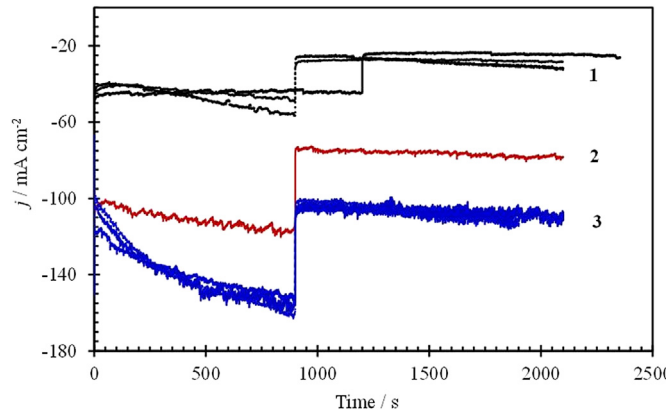


**Fig. 1.** Typical  $j(t)$  curves measured during Ni–Mn catalysts electrodeposition from B3 bath at applied potential  $E_1 = -1.2/\text{V}$  vs SCE followed by  $E_2 = -1.1/\text{V}$  vs SCE; 1)  $T_{\text{bath}} = 26.5^\circ\text{C}$ , 2)  $T_{\text{bath}} = 51.5^\circ\text{C}$ , and 3)  $T_{\text{bath}} = 61^\circ\text{C}$ .

$$I_p = \kappa n^{3/2} D^{1/2} C^* S_M V_b^{1/2} = p_M V_b^{1/2} \quad (2)$$

where  $D$  and  $C^*$  are the diffusion coefficient and the bulk concentration of the reacting species, respectively.  $n$  is the change number of the electrode determined reaction step,  $V_b$  the potential scan rate,  $S_M$  the ECSA of each electrode M,  $\kappa$  a numerical constant which is determined empirically and  $p_M$  the slope of the straight line  $I_p$  against  $V_b^{1/2}$  and which can be expressed as follow: for Pt electrode

$$p_{\text{Pt}} = \frac{dI_p}{dV_b^{1/2}} = \kappa n^{3/2} D^{1/2} C^* S_{\text{Pt}} \quad (3)$$

for an electrode material M

$$p_M = \frac{dI_p}{dV_b^{1/2}} = \kappa n^{3/2} D^{1/2} C^* S_M \quad (4)$$

Hence for each electrode M the ECSA corresponds to

$$S_M = S_{\text{Pt}} \frac{p_M}{p_{\text{Pt}}} \quad (5)$$

To evaluate the ECSA for each electrode,  $S_M$ , from CV measurements at various potential scan rates, the ferri-ferrocyanide system in basic media has been used.

### 3. Results and discussion

#### 3.1. Ni–Mn films deposition

In the first step, Ni–Mn films were electrodeposited for different conditions of bath composition and temperature using two successive polarization potential values. In this work the deposition procedure have been conducted at constant potential  $E_1 = -1.2/\text{V}$  vs SCE and after at  $E_2 = -1.1/\text{V}$  vs SCE (Fig. 1). Under potential  $E_1$ , deposition reaction is accompanied by hydrogen production at high level. Consequently, the  $\text{H}_2$  bubbles burning at the electrode surface produce some tensions in the bulk of the deposit leading to cracked surface. In addition, the gas release generates turbulence near the electrode and heterogeneous diffusion of metallic ions occurs [31] therefore the time-current density curve grows continually (Fig. 1). Under  $E_2$ , the  $\text{H}_2$  bubbles production decreases strongly leading to quiescent medium, the surface cracks seems to be collapsed and the current density seems to be stabilized around constant value.

The reproducibility of the measurements was verified by repetitions of some experiments in the same operating conditions. As it is shown in Fig. 1 where typical different deposits are synthesized at two operating temperature, namely  $T_{\text{bath}} = 26.5^\circ\text{C}$  and  $61^\circ\text{C}$  and the corresponding Ni–Mn coatings are so-called respectively, NiMn25C ( $T_{\text{bath}} = 26.5^\circ\text{C}$ ) and NiMn60C ( $T_{\text{bath}} = 61^\circ\text{C}$ ). From the figure, it is clear that the  $j$ -time curves show an acceptable reproducibility.

Fig. 2 shows the SEM images of freshly deposited films for various bath temperatures. It is clear that the deposit morphology changed strongly for high temperature values. At low temperatures ( $T_{\text{bath}} = 19^\circ\text{C}$  and  $26.5^\circ\text{C}$ ) the surface morphology appears smooth and fairly compact with number of cracks. The obtained results look like SEM mages of Ni–Mn coating previously reported in Ref. [20]. When  $T_{\text{bath}}$  increases the micrographs show that three dimensional aspect of the deposit progressively appears at  $T_{\text{bath}} \geq 60^\circ\text{C}$  with pores and nodules everywhere in the surface. The number of cracks

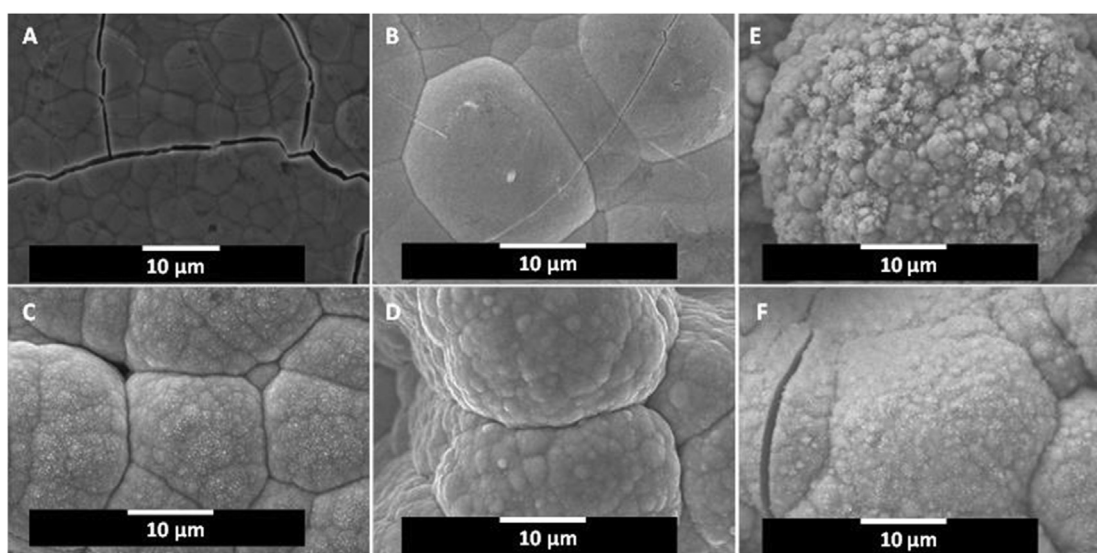


**Fig. 2.** SEM micrographs after electrodeposition of Ni–Mn alloys prepared at constant potentials corresponding to Fig. 1 ( $E_1 = -1.2/\text{V}$  vs SCE,  $\Delta t_1 = 15 \text{ min}$  and  $E_2 = -1.1/\text{V}$  vs SCE,  $\Delta t_2 = 20 \text{ min}$ ) from bath B3 and for various  $T_{\text{bath}}$  values. (A):  $T_{\text{bath}} = 19^\circ\text{C}$ ; (B):  $T_{\text{bath}} = 26.5^\circ\text{C}$ ; (C):  $T_{\text{bath}} = 51.5^\circ\text{C}$ ; (D)  $T_{\text{bath}} = 61^\circ\text{C}$ . (E) and (F) SEM micrographs of NiMn60C catalysts after cycling at constant cell voltage  $\Delta E = \pm 2.5 \text{ V}$  (see Fig. 11), when the cycling experiment was stopped after anodic polarization (E) or after cathodic polarization (F).

decreases significantly leading to more compact morphology. The increase of  $T_{\text{bath}}$  leads to spongy coating with high porosity and more granular aspect (see Fig. 3). Thus the active surface and consequently the catalytic active sites number are increased to high level. In Fig. 3, we have also reported the pictures of two NiMn60C deposits obtained in the same operating conditions. From this, it is noteworthy that the same aspect of the as prepared samples is observed. The surface morphology modifications appearing at high temperature may be related to both the increase of nucleation rate with temperature and to the hydrodynamic regime inside the electrochemical cell modifications due to hydrogen evolution [32]. By increasing the temperature the HER rate increases leading to the solution stirring near the electrode at high level. The holes between the agglomerates of grains are due to the large coverage with hydrogen bubbles.

In Table 2 the weight percentage ratios of Ni and Mn, seems to be the same for various temperatures. Nevertheless, the composition values are in the same order as that reported in previous works [16,22,23].

From the hatched area of CV measurements reported in Fig. 4A and using Eq. (3), the ECSA,  $S_{\text{Pt}}$  is determined in the case of Pt

**Table 2**

Nickel and manganese content deduced from EDX analysis of the Ni–Mn catalysts deposited at various bath temperature.

Element	Bath temperature			
	19 °C	26.5 °C	51.5 °C	61 °C
Ni	95.3	95.4	94.9	95.5
Mn	4.7	4.6	5.1	4.5

electrode. While the ECSA of the other electrodes,  $S_M$  are calculated using Eq. (5) and the slopes  $p_{\text{Pt}}$  and  $p_M$  deduced from the  $I_p = f(V_b^{1/2})$  representation shown in Fig. 4B. The obtained data are reported in Table 3. We have also reported the equivalence of ECSA in term of the Pt catalyst mass loading evaluated according to [29]. From the table, it is worth noting that the analysis of obtained data confirmed that the ECSA modifications were directly related to the temperature. It is also important to note that the NiMn60C deposits exhibit the high ECSA value. This amplification is in accordance with surface morphology of such deposits where the presence of large holes or craters between cauliflower-like grains is clearly shown on the images reported in Fig. 3.

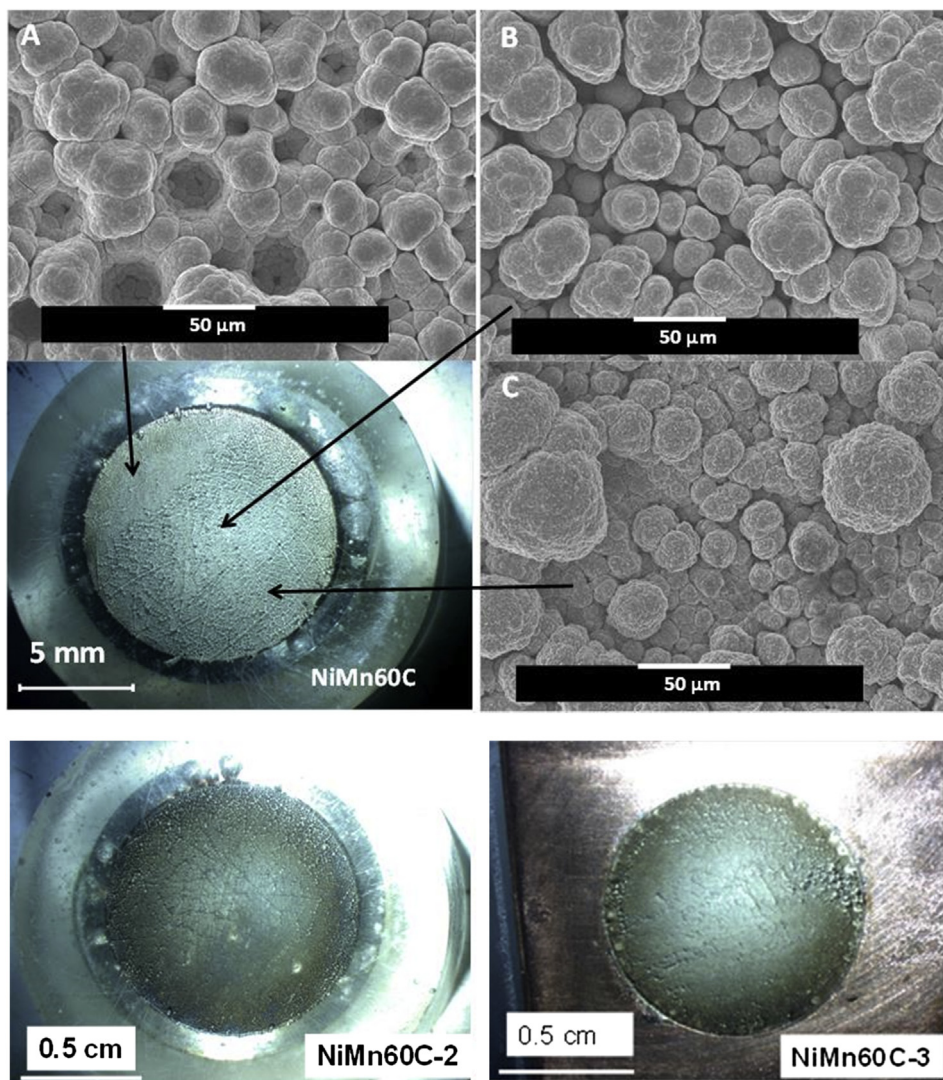


**Fig. 3.** Picture of WE recovered with NiMn60C catalyst and typical SEM images of different positions of the surface after electrodeposition from B3 bath at  $T_{\text{bath}} = 61^{\circ}\text{C}$  according to Fig. 1.

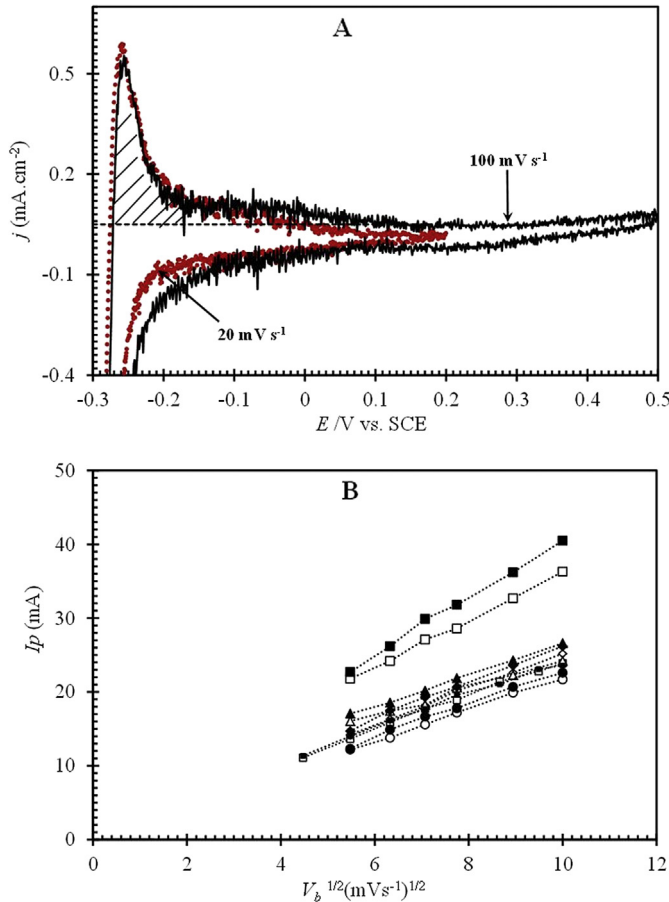


**Fig. 4.** A. Cyclic voltammograms of Pt electrode immersed in 1 M H<sub>2</sub>SO<sub>4</sub> solution at scan rate  $V_b = 20 \text{ mV s}^{-1}$  (red curve)  $V_b = 100 \text{ mV s}^{-1}$  (black curve). B. The relationship between  $V_b^{1/2}$  and the peak current,  $I_p$ , measured in anodic (full symbols) and cathodic (empty symbols) scanning for various catalysts in 1 M KOH + 0.1 M K<sub>3</sub>Fe(CN)<sub>6</sub>/K<sub>2</sub>Fe(CN)<sub>6</sub> solution.  $T_{\text{bath}} = 22.5^\circ\text{C}$ . (■, □): Pt; (●, ○): Ni; (◆, ◇): Mn; (△, ▲): NiMn25C; (■, □): NiMn60C. (For interpretation of the references to colour in this figure legend, the reader is referred to the web version of this article.)

### 3.2. HER reaction

To compare the performance of Ni–Mn deposits for HER, the same experiments were performed using commercial massive platinum electrode, electrodeposited Ni coating and electro-deposited Mn coating. From Fig. 5, it is clear that the binary Ni–Mn coating NiMn25C has higher HER activity than Ni, Mn coating and Pt massive electrode. In addition for the Ni–Mn coating deposited at high temperature (i.e. NiMn60C), the HER activity is higher than other catalysts. All electrodes show a typical Tafel behavior indicating that the HER is under kinetic control (Fig. 5C). The Tafel slope

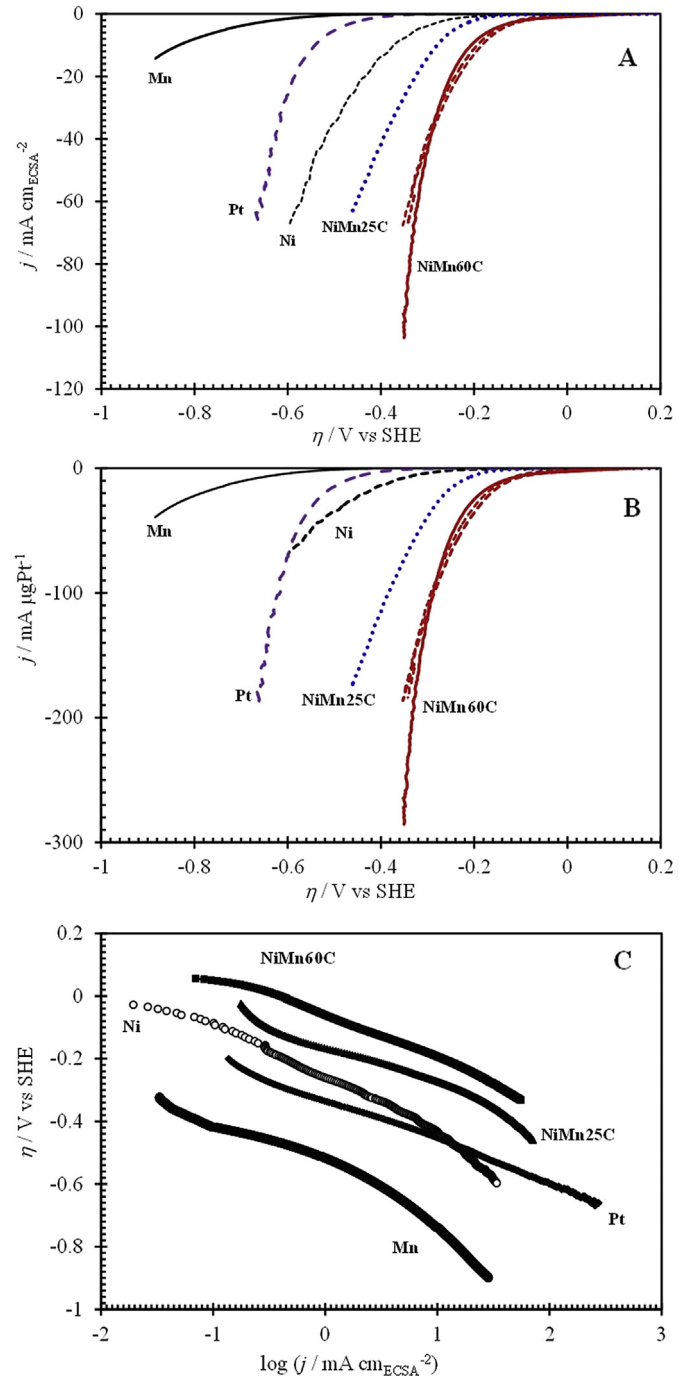


**Fig. 5.** A & B. Polarization curves measured during HER in 1 M NaOH for various catalysts at scan rate  $V_b = 0.5 \text{ mV s}^{-1}$  and  $T_{\text{bath}} = 26.5^\circ\text{C}$ . Ni was obtained from bath B1 at  $E = -1.1/\text{V}$  vs SCE,  $\Delta t = 30 \text{ min}$ ,  $Q = 27 \text{ C cm}^{-2}$ . Mn deposit was obtained from bath B2 at  $E = -2.0/\text{V}$  vs SCE,  $\Delta t = 30 \text{ min}$ ,  $Q = 60 \text{ C cm}^{-2}$  ( $Q$  is the electricity amount). NiMn25C and NiMn60C are prepared from bath B3 and the corresponding CD-time dependence curves are reported in Fig. 1. C. HER Tafel plots corresponding to the polarization curves reported in Fig. 5A. Overpotential  $\eta = (E - IR) - E_{\text{rev}}$  ( $\text{pH} = 14.1$ ) (were  $E$  is the applied potential).

is changing from 91 mV dec<sup>-1</sup> (for NiMn25C coating) to 202 mV dec<sup>-1</sup> in the case of Mn coating (see Table 4) and the exchange current density (ECD),  $j_0$ , values are in the range of 0.264 and 21.1  $\mu\text{A cm}^{-2}$  for Pt, Ni, Mn and NiMn25C electrodes. However the NiMn60C catalyst exhibits an ECD value more than 40 times higher indicating the high catalytic activity of this coating. Another

**Table 3**  
Geometric surface, experimental ECSA and Pt mass loading of electrodes.

Electrode	Pt	Cu/Ni	Cu/Mn	Cu/NiMn25C	Cu/NiMn60C
Geometric surface area/cm <sup>2</sup>	1.038	1.038	1.038	1.038	1.038
ECSA calculated from $I_{pc}/\text{cm}^2$	1.925	1.799	2.027	1.804	2.675
ECSA calculated from $I_{pa}/\text{cm}^2$	1.925	1.940	2.142	1.847	3.355
ECSA mean value/cm <sup>2</sup>	1.925	1.870	2.084	1.825	3.015
m (Pt)/ $\mu\text{g}$	0.6988	0.6788	0.7567	0.6626	1.094

**Table 4**

HER kinetic parameters obtained from Tafel representation of the experimental  $j(\eta)$  curves reported in Fig. 5.

Catalyst	Mn	Ni	Pt	NiMn25C	NiMn60C
	$b/\text{mV dec}^{-1}$	$j_0/\mu\text{A cm}^{-2}$	$j_0/\mu\text{A cm}_{\text{ECSA}}^{-2}$	$-\eta_{-25}/\text{mV}$	$P/\text{mW cm}^{-2}$
Mn	202	167	112	91.0	143
Pt	3.27	38.0	0.49	23.0	1120
NiMn25C	1.63	21.1	0.264	13.0	385
NiMn60C	865	515	563	300	183
$P/\text{mW cm}^{-2}$	21.6	12.9	14.1	7.50	4.57

way to compare the catalytic activity of catalyst is to determine the overpotential of each catalyst at given current density (CD). This would give an indication on the amount of energy that has to be invested to produce a fixed amount of hydrogen [10]. In Table 4, the overpotential values measured at fixed CD of  $j = 25 \text{ mA cm}^{-2}$  and the corresponding power are reported. From the table it is clear that among the catalysts investigated here, the Ni–Mn catalysts need more less power impute (i.e. for NiMn25C tow times lower and three times less for NiMn60C than massive Pt electrode). In Fig. 5 and for Tafel representations, the overpotential,  $\eta$ , data were ohmic drop corrected with respect to the reversible HER potential at the given conditions ( $E_{\text{rev}} = -0.832/\text{V}$  vs SHE in 1 M NaOH, pH = 14.1) and the solution resistance,  $R_s$ , value was determined from the EIS measurements (see below). It should be noted that, due to active surface variations between the catalysts investigated in this work, all CD values are calculated using the geometric area of each working electrode.

Electrochemical impedance spectroscopy (EIS) is one good tool to study the electrode reactions kinetics. Based on disruption method, this technique is able to probing relaxation processes over a large frequency domain. EIS measurements were carried out after deposition procedure in order to check the processes occurring at the catalyst/solution interface when electrode potential is varied. We present bellow a partial analysis of experimental data obtained using NiMn60C catalyst during HER in 1 M NaOH and EOR in 1 M ethanol and 1 M NaOH.

Generally EIS data are presented in the so-called Nyquist diagram were imaginary vs real parts are plotted for measurement frequencies. Fig. 6 shows the Nyquist diagrams of NiMn60C catalyst during HER at various cathodic applied potential,  $E$ . The obtained

diagrams are similar to that previously obtained for HER using other Ni based catalysts [10–12]. The data clearly reveal the presence of two slight depressed capacitive loops. The high frequency capacitive loop corresponds to the charges transfer processes combined with double layer charging process and the low frequency loop may be attributed to the adsorption on the electrode surface of reaction intermediate (e.g.  $H_{\text{ad}}$  which is generally admit as intermediate in Volmer–Herowsky or Tafel mechanisms of HER). Both loops are strongly modified with increasing  $E$  values.

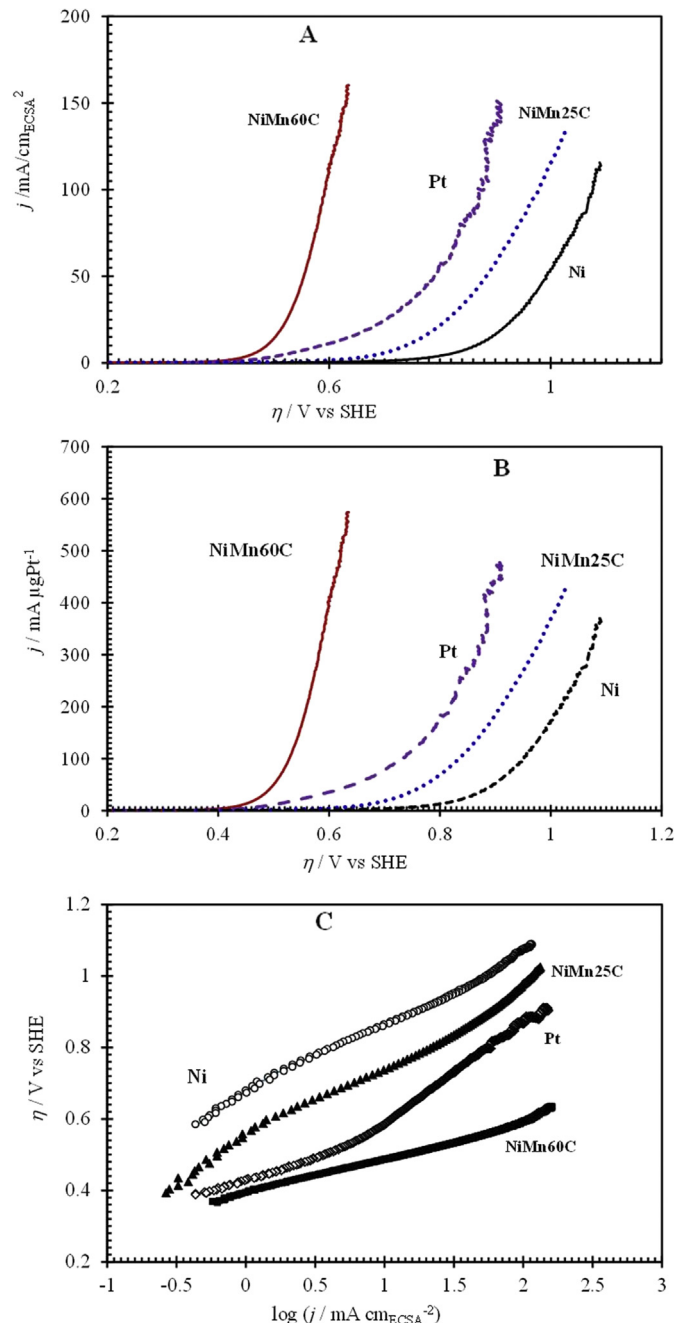


**Fig. 7.** A & B. Polarization curves measured during OER in 1 M NaOH for the same catalysts as in Fig. 2. Potential scan rate  $V_b = 0.5 \text{ mV s}^{-1}$  and  $T_{\text{bath}} = 26.5 \text{ }^\circ\text{C}$ . Overpotential is calculated as:  $\eta = E - IR_s - E_{\text{rev}}$  (pH = 14.1) (were  $E$  is the applied potential and  $R_s$  is the solution resistance). C. Tafel plots corresponding to the OER in 1 M NaOH for the same catalysts as in Fig. 2. Potential scan rate  $V_b = 0.5 \text{ mV s}^{-1}$  and  $T_{\text{bath}} = 26.5 \text{ }^\circ\text{C}$ .

**Fig. 6.** Nyquist plots of the impedance diagrams measured on NiMn60C catalyst in the case of HER at different applied potential.  $[\text{NaOH}] = 1 \text{ M}$  and  $T_{\text{bath}} = 26.5 \text{ }^\circ\text{C}$ . (●):  $E = -1.30/\text{V}$  vs SCE; (○):  $E = -1.40/\text{V}$  vs SCE; (▲):  $E = -1.50/\text{V}$  vs SCE; (◊):  $E = -1.60/\text{V}$  vs SCE.

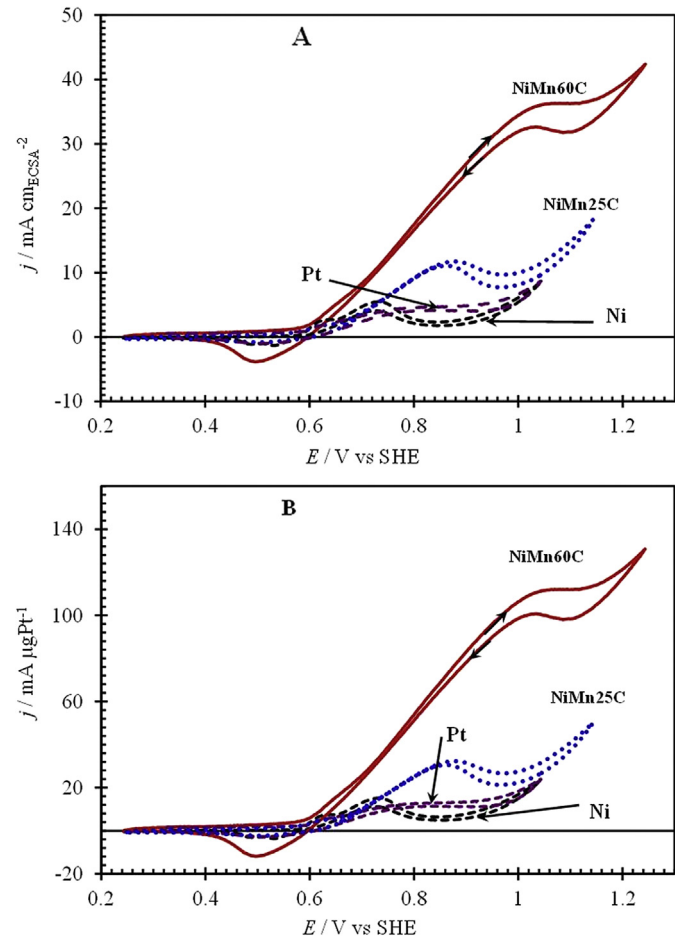
### 3.3. Oxygen evolution reaction

Oxygen evolution reaction (OER) is one of the most widely studied reactions in the field of electro-catalysis [33–38]. To improve oxygen kinetics and durability of the electrode, extensive studies for highly active and stable oxygen electro-catalysts have been performed [37]. The current density overpotential curves and Tafel plots measured on Ni, Pt, NiMn25C and NiMn60C anodes are shown in Fig. 7. As seen in Fig. 7A, in the case of NiMn60C anode, the current passing through the solution increases after a small potential is applied. However for Ni anode a high potential value is needed to produce electrolysis current. All polarization curves are corrected from ohmic drop effect with respect to the reversible OER potential ( $E_{rev} = 0.398$  V vs SHE in 1 M NaOH, pH = 14.1). In Table 5 we have reported the OER kinetic parameters deduced from the Tafel representation of Fig. 7C. From the Table it is clear that the NiMn60C catalysts exhibit a low (ECD),  $j_0$  value and low Tafel slope. A Tafel slope around of 120 mV dec<sup>-1</sup> is generally attributed to the dissociative water adsorption with release of a proton and electron. The low Tafel slope may be attributed to the presence of adsorbed intermediates on the surface with different energy states. Any rigorous kinetic analysis of the OER lies beyond the topic of the present work. Rather, we focus mainly on efficiency modification of electrochemical conversion of H<sub>2</sub>O to O<sub>2</sub>. The comparison of the resulting overpotential values at fixed CD of  $j = 200$  mA cm<sup>-2</sup> may give some indications on the amount of energy that has to be invested to produce a fixed oxygen amount. From Table 5 it is obvious that NiMn60C catalyst requires the lowest energy input for the given oxygen amount production i.e. almost 53% lower than Ni and 58% than Pt.

### 3.4. Ethanol oxidation reaction (EOR)

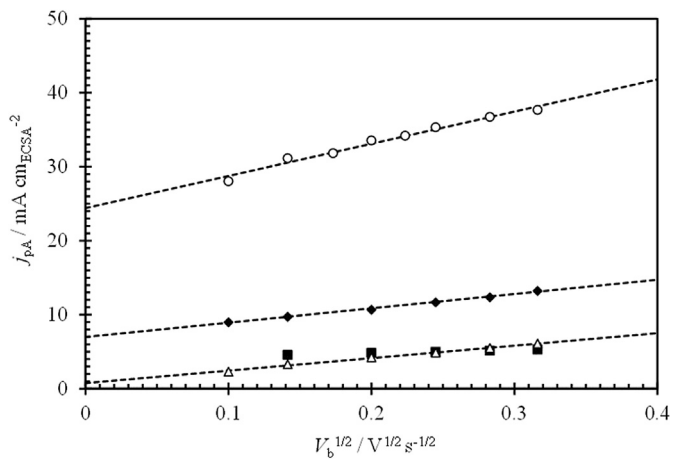
Ethanol is a renewable and attractive fuel as it can be produced in great quantities from biomass and it is less toxic than methanol. However, its complete oxidation to CO<sub>2</sub> is more difficult due to the difficulty in C–C bond breaking and to the formation of CO-intermediates that poison the platinum anode catalysts. In this context, more active electro-catalysts are essential to enhance the EOR [39–46]. An extensive review of catalysts composition for application in direct ethanol fuel cell has been published by Kamarudin et al. [40] and reported that in most cases, anode and cathode catalysts are based on precious metal such as Pt, Pd, Ru or Ir.

Fig. 8 shows the CV diagrams of EOR on the as-prepared catalysts and massive Pt in 1 M C<sub>2</sub>H<sub>5</sub>OH and 1 M NaOH at potential scan rate  $V_b = 100$  mV s<sup>-1</sup>. The obtained CVs are similar to those reported in the literature [39,42] with two irreversible current peaks which are typically attributed to ethanol electro-oxidation. In forward scan, the oxidation peaks are around  $E_{pf} \approx 1.0$  V vs SHE on NiMn60C,  $E_{pf} \approx 0.85$  V vs SHE on NiMn25C,  $E_{pf} \approx 0.81$  V vs SHE on Pt and  $E_{pf} \approx 0.72$  V vs SHE on Ni. In the backward scan the re-



**Fig. 8.** A & B. Cyclic voltammetry curves measured during 1 M ethanol oxidation in 1 M NaOH for the same catalysts as in Fig. 2. Potential scan rate:  $V_b = 100$  mV s<sup>-1</sup> and  $T_{bath} = 26.5$  °C.

oxidation of ethanol occurs at practically the same  $E_p$  values for each catalyst. The peak current density toward ethanol oxidation on the four catalysts has the following order: NiMn60C (34.3 mA cm<sup>-2</sup>) > NiMn25C (11.6 mA cm<sup>-2</sup>) > Ni (6.1 mA cm<sup>-2</sup>) ≈ Pt (5.3 mA cm<sup>-2</sup>). As for HER and OER



**Fig. 9.** The relationship between the forward oxidation peak CD values and square root of potential scan rate measured during ethanol oxidation on various catalysts in 1 M EtOH + 1 M NaOH.  $T_{bath} = 26.5$  °C. (■): Pt; (Δ): Ni; (◆): NiMn25C; (○): NiMn60C.

**Table 5**

OER kinetic parameters obtained from Tafel representation of the experimental  $j(\eta)$  curves reported in Fig. 7.

Catalyst				
	Ni	Pt	NiMn25C	NiMn60C
$b/\text{mV dec}^{-1}$	165	121	151	90.7
$j_0/\text{mA cm}^{-2}$	0.10	0.50	0.44	0.11
$j_0/\text{mA cm}^{-2}$	0.055	0.270	0.250	0.038
$\eta_{-200}/\text{V}$	1.09	0.997	0.885	0.573
$P/\text{mW cm}^{-2}$	218	200	177	115
$P/P_{Ni}/\%$	100	91.6	81.3	52.7

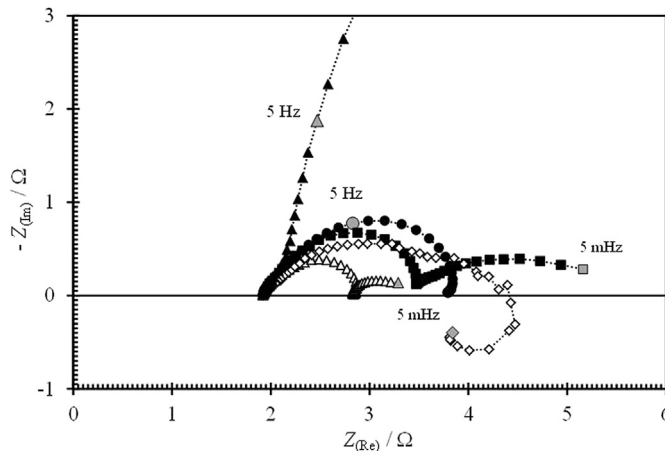


**Fig. 10.** Nyquist plots of the impedance diagrams measured on NiMn60C catalyst in the case of EOR at different applied potential.  $[EtOH] = 1\text{ M}$ ;  $[NaOH] = 1\text{ M}$  and  $T_{bath} = 26.5\text{ }^\circ\text{C}$ . (●):  $E = 0.40/\text{V}$  vs SCE; (Δ):  $E = 0.50/\text{V}$  vs SCE; (■):  $E = 0.60/\text{V}$  vs SCE; (◊):  $E = 0.80/\text{V}$  vs SCE.

discussed above, we confirm here that alloying Ni with Mn leads to better catalytic activity than Pt or Ni alone during EOR. The NiMn60C catalyst gives the highest peak CD, (i.e. 10 times higher compared to Pt or Ni catalysts) indicating that NiMn60C catalyst is

significantly more active for ethanol oxidation in basic media. On the other hand the peak currents are proportional to the square root of potential scan rate on all catalysts and the straight line  $j_p/\text{A}$  vs  $V_b^{1/2}$  has a high level for NiMn60C catalysts (see Fig. 9). Due to the larger effective active surface of NiMn60C which is obviously greater than the geometric area the catalysts give a larger interface, and higher catalytic activity.

In Fig. 10, we have reported typical EIS measurements obtained during EOR on NiMn60C for various applied potential values. The data remain the EIS diagrams previously obtained using Pt electrode [42,46] and indicate that electro-oxidation of ethanol on NiMn60C catalysts exhibit different impedance behaviors when applied potential is varied. Therefore, the EIS data reveal that the EOR mechanism on Ni–Mn based catalysts involves the formation of intermediate species and the rates determine step change with applied potential value.

### 3.5. Stability of NiMn60C catalysts

Preliminary stability test of the NiMn60C catalysts have been carried out by current cycling (polarization at constant applied current  $I = -25\text{ mA}$  during one hour followed by polarization at applied constant current  $I = +25\text{ mA}$  during one hour and vice versa). The test has been conducted during 40 h at  $T_{bath} = 26.5\text{ }^\circ\text{C}$

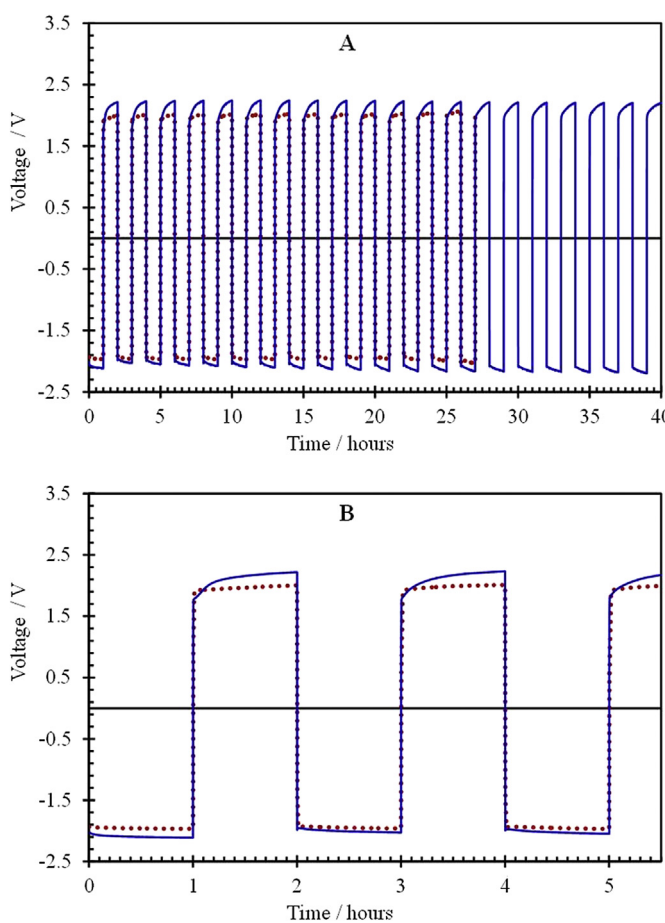


**Fig. 11.** A. Typical cell voltage cycling measured on NiMn60C catalysts in 1 M NaOH under applied constant current  $I = \pm 25\text{ mA}$  at  $T_{bath} = 26.5\text{ }^\circ\text{C}$  (blue full line) and  $T_{bath} = 51.5\text{ }^\circ\text{C}$  (red dotted line). B. Expansion of the cell voltage cycling curves in Fig. 11A. (For interpretation of the references to colour in this figure legend, the reader is referred to the web version of this article.)

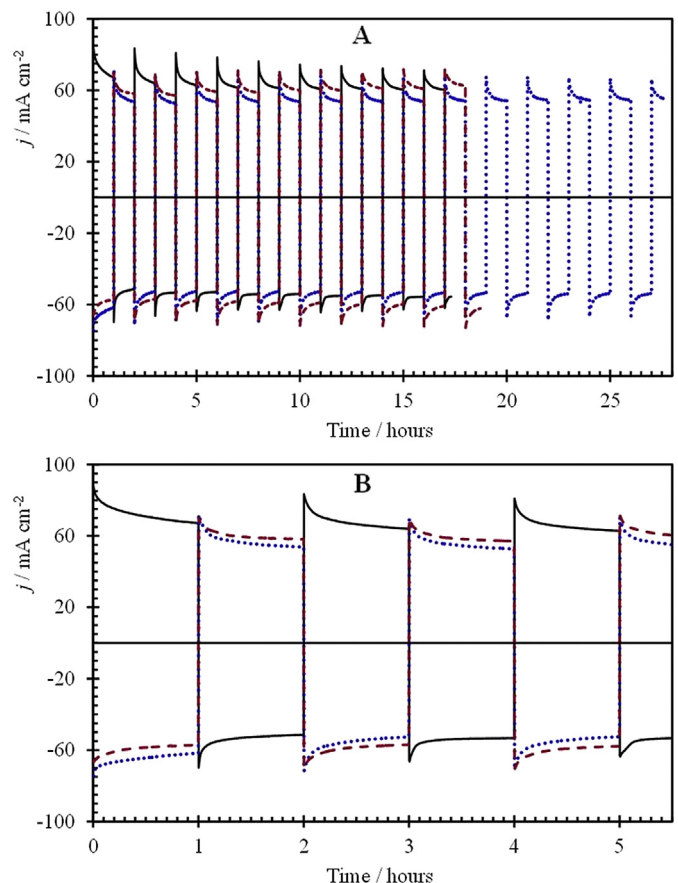


**Fig. 12.** A. Typical current density response for cycling under applied constant voltage  $\Delta E = \pm 2.5\text{ V}$  measured on NiMn60C catalysts in 1 M NaOH at  $T_{bath} = 26.5\text{ }^\circ\text{C}$  and for three tests: Full line (black); dotted line (blue); second test and dashed line (red); third test. B. Expansion of the response for cycling under applied constant voltage  $\Delta E = \pm 2.5\text{ V}$  measured on NiMn60C catalysts in 1 M NaOH at  $T_{bath} = 26.5\text{ }^\circ\text{C}$  and for three tests: Full line (black); dotted line (blue); second test and dashed line (red); third test. (For interpretation of the references to colour in this figure legend, the reader is referred to the web version of this article.)

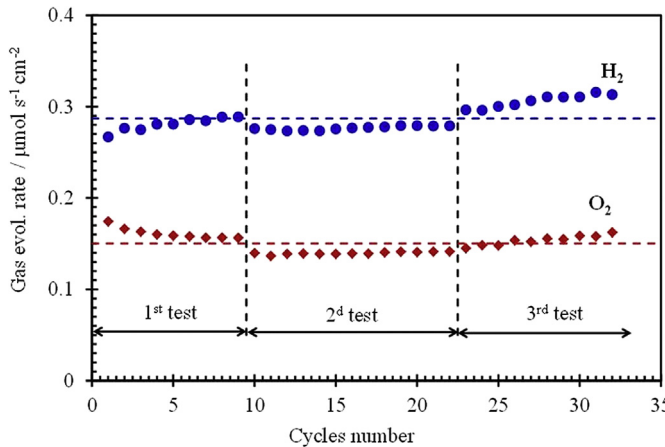


**Fig. 13.** Gas evolution rate of hydrogen (blue) and oxygen (red) production, calculated from the results reported in Fig. 12 and according to Eq. (8). The cycle corresponds to duration  $\Delta t = 2$  h. (For interpretation of the references to colour in this figure legend, the reader is referred to the web version of this article.)

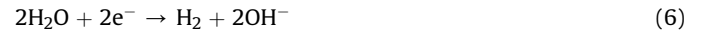
and 27 h after at  $T_{\text{bath}} = 51.5$  °C. In Fig. 11A, the cell voltage responses have been reported for  $T_{\text{bath}} = 26.5$  °C (solid line) and for  $T_{\text{bath}} = 51.5$  °C (dotted line). In the two cases, the cell exhibits a very stable voltage over long time. At high temperature the voltage seems to reach rapidly a constant value in accordance with reaction kinetics enhancement due to the temperature increase (Fig. 11B). The stationary voltage values decrease when  $T_{\text{bath}}$  increases (e.g. in Fig. 11B at  $t = 4$  h:  $\Delta E = +2.20$  V when  $T_{\text{bath}} = 26.5$  °C and  $\Delta E = +1.98$  V when  $T_{\text{bath}} = 51.5$  °C), this fact may be attribute to the decrease of the cell ohmic drop at high temperature [47].

We have also examine the NiMn60C performance under cell voltage cycling (each cycle corresponds to a constant polarization at  $\Delta E = -2.5$  V during one hour followed by a constant polarization at  $\Delta E = +2.5$  V during one hour and vice versa) and three tests have been successively conducted with the same pair of electrodes in the electrolytic solution. Fig. 12 shows the CD-time transients obtained

for NiMn60C catalysts in 1 M NaOH at  $T_{\text{bath}} = 26.5$  °C. From Fig. 12B it is clear that the same transient shape is obtained and the average CD values remain practically the same during the three tests in cathodic mode.

Assuming that all of the anodic current was caused by  $4e^-$  oxidation of water to produce  $O_2$  and cathodic current was caused by  $2e^-$  reduction of water to produce  $H_2$ , the gas evolution rates of  $H_2$  and  $O_2$  during water electrolysis may be calculated using the measured CD,  $j/\text{A cm}^{-2}$  passing from the cell for a period of time  $\Delta t/\text{s}$  and the number of exchanged electron during the global reactions.

At the cathode:



At the anode:



The gas evolution rates are calculated as follow:

$$\Delta n(H_2)/\Delta t = j/2F \text{ and } \Delta n(O_2)/\Delta t = j/4F \quad (8)$$

In these equations the Faraday constant was  $F = 96,500 \text{ C mol}^{-1}$  and  $\Delta n_i$  corresponds to the moles amount produced for each gas  $i$ . In Fig. 13, the variation of  $H_2$  and  $O_2$  gas evolution rates calculated according to Eq. (8) are given vs the cycle number.

In summary from these preliminary tests, we can say that in 1 M NaOH solution at  $T_{\text{bath}} = 26.5$  °C or 51.5 °C, the cell performance test at constant current or constant cell voltage, shows a good stability of the NiMn60C catalysts in anodic or cathodic mode. During voltage cycling, the cathodic current remains practically the same during the three tests (Fig. 12). However anodic current seems to increase during the third test and the electrode surface seems to be coated with some black products (see the video in supplementary elements). In fact during the third test a black aspect of the electrode appears clearly during the anodic polarization ( $\Delta E = +2.5$  V) and disappears during the cathodic polarization ( $\Delta E = -2.5$  V) or if

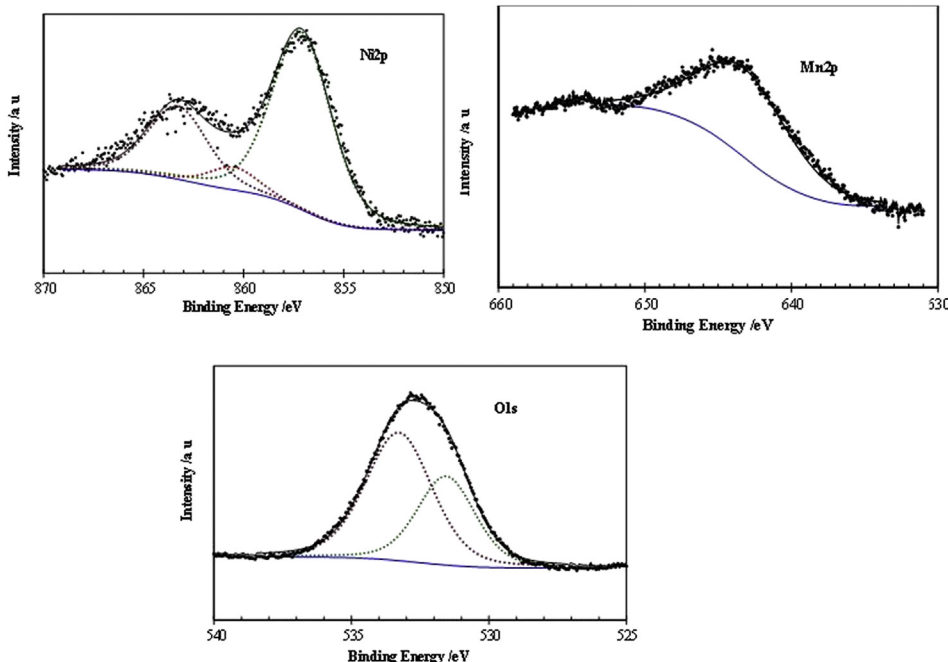


**Fig. 14.** High resolution XPS Ni2p, Mn2p and O1s spectra of NiMn60C electrode after potentiostatic polarization at  $\Delta E = +2.5$  V in 1 M NaOH at  $T_{\text{bath}} = 26.5$  °C.

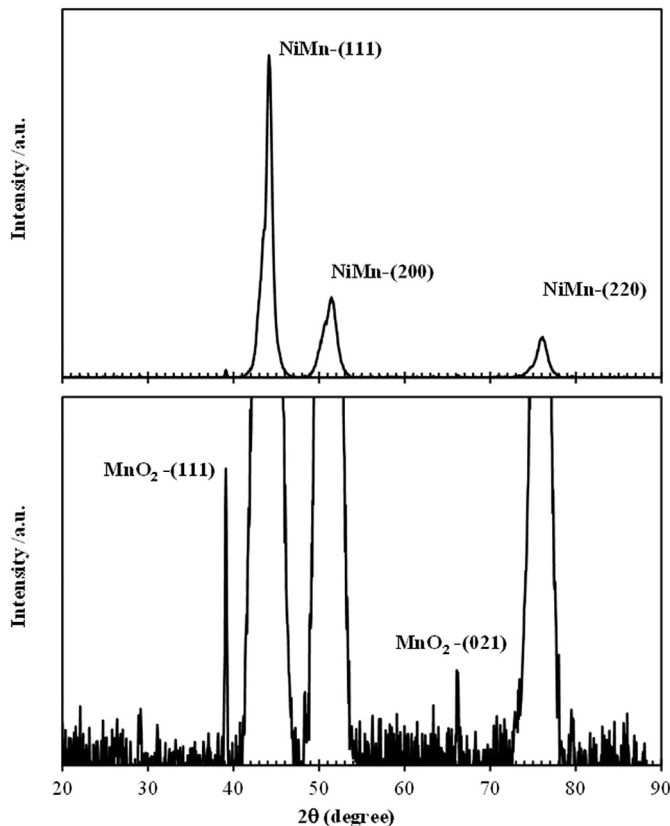


**Fig. 15.** High resolution X-ray patterns of NiMn60C electrode after potentiostatic polarization at  $\Delta E = +2.5$  V for 1 h in 1 M NaOH at  $T_{\text{bath}} = 26.5$  °C.

we take the electrode out the cell and rinse it with acidic solution. The chemical composition of the black layer has been analyzed by XPS and XRD investigations. The detailed XPS spectra of the sample (Fig. 14) shows that typical Ni2p signal is found in the range 854.9 eV, Mn2p signal appears in the range of 641.4 eV and O1s signal is clearly identified at 531.2 eV [48,49]. In Fig. 15 we have reported the high resolution of the XRD pattern of the NiMn60C electrode recovered with black layer. According to [49–51] the peaks appearing at  $2\theta = 38.9^\circ$  and  $2\theta = 66.1^\circ$  may be attributed to  $\text{MnO}_2$  layer (Fig. 15). It must be noted that from these analysis the black layer is mainly composed of  $\text{Ni}(\text{OH})_2$  and  $\text{MnO}_2$ .

Supplementary video related to this article can be found at <http://dx.doi.org/10.1016/j.jpowsour.2014.06.145>.

Therefore, due to the existence  $\text{Ni}(\text{OH})_2$  and  $\text{MnO}_2$  layer the gas evolution rate of water electrolysis slightly increases (about 6% for production of  $\text{H}_2$  and 12% for  $\text{O}_2$  production (see Fig. 13) over the last 10 cycles and the catalysts spongy aspect remains practically unchanged (see SEM images E and F in Fig. 2). From a surface reactivity standpoint, fruitful kinetic synergy between the oxides layer and NiMn60C catalyst appears to be the key to maximizing the rate of the OER as it was observed in Ref. [13] in the case of  $\text{Ni}(\text{OH})_2$  during HER.

#### 4. Conclusion

In this work we show a new way to produce catalyst materials by varying the polarization potential sequence and essentially the modification of bath temperature. The operating deposition conditions were optimized to produce Ni–Mn coatings with high active surface (e.g. spongy aspect). The outstanding catalytic activity and the durability of the catalysts have been characterized in

basic media using several electrochemical processes, such as hydrogen evolution reaction (HER), water oxidation reaction (OER) and ethanol oxidation reaction (EOR).

As a matter of fact the best performance of our Ni–Mn based catalysts for HER, OER and EOR could be due to the modification of tow parameters: the real electrocatalytic activity changes through an enhancement of the suitability of the active sites by inducing Mn in the Ni alloy and the increase of the real effective surface area (high porosity and roughness) resulting from the increase of deposition bath temperature more than 60 °C. The porosity of the surface layer contributes substantially to an enlargement of the electrode real active surface area and to the active sites number. Spongy structure and high active surface area of NiMn60C catalysts favors their use as new low cost and versatile electro-catalytic materials.

#### References

- [1] K. Hall, Compr. Renew. Energy 4 (2012) 351–360.
- [2] G. Wu, L.K. More, M.C. Johnston, P. Zelenay, Science 332 (2011) 443–447.
- [3] S. Dunn, Int. J. Hydrogen Energy 27 (2002) 235–264.
- [4] I. Dincer, Int. J. Hydrogen Energy 27 (2002) 265–285.
- [5] P. Thounthong, S. Rael, B. Davat, J. Power Sources 158 (2006) 806–814.
- [6] S. Cobo, J. Heidkamp, P.-A. Jacques, J. Fize, V. Fourmond, L. Guetaz, B. Josselme, V. Ivanova, H. Dau, S. Palacin, M. Fontecave, V. Artero, Nat. Mater. 11 (2012) 802–807.
- [7] B.D. James, J.A. Kalinoski, DOE Hydrogen Program, FY 2008 Annual Progress Report, 2008, pp. 798–802.
- [8] Johnson Matthey, <http://www.platinum.matthey.com/prices/price-charts>.
- [9] K. Kendall, B.G. Pollet, Compr. Renew. Energy 4 (2012) 301–313.
- [10] E. Navarro-Flores, Z. Chong, S. Omanovic, J. Mol. Catal. A Chem. 226 (2005) 179–197.
- [11] L. Birry, A. Lasia, J. Appl. Electrochem. 34 (2004) 735–749.
- [12] O. Aaboubi, Int. J. Hydrogen Energy 36 (2011) 4702–4709.
- [13] R. Subbaraman, D. Tripkovic, D. Strmcnik, K.C. Chang, M. Uchimura, A.P. Paulikas, V. Stamenkovic, N.M. Markovic, Science 334 (2011) 1256–1260.
- [14] A. Stephen, M.V. Ananth, V. Ravichandran, B.R.V. Narashiman, J. Appl. Electrochem. 30 (2000) 1313–1316.
- [15] S.H. Goods, J.J. Kelly, N.Y.C. Yang, Microsyst. Technol. 10 (2004) 498–505.
- [16] R. Fathi, S. Sanjabi, Curr. Appl. Phys. 12 (2012) 89–92.
- [17] A. Stephen, F. Rossi, L. Nasi, C. Ferrari, N. Ponpandian, M.V. Ananth, V. Ravichandran, J. Appl. Phys. 103 (2008) 053511-1–053511-7.
- [18] E.A. Marquis, A.A. Talin, J.J. Kelly, S.H. Goods, J.R. Michael, J. Appl. Electrochem. 36 (2006) 669–676.
- [19] A.A. Talin, E.A. Marquis, S.H. Goods, J.J. Kelly, M.K. Miller, Acta Mater. 54 (2006) 1935–1947.
- [20] A. Stephen, D. Kalpana, M.V. Ananth, V. Ravichandran, Int. J. Hydrogen Energy 24 (1999) 1059–1066.
- [21] M.V. Ananth, P. Ananthi, Int. J. Hydrogen Energy 33 (2008) 5779–5788.
- [22] A.O. Yüce, A. Döner, G. Kardaş, Int. J. Hydrogen Energy 38 (2008) 12102–12111.
- [23] I. Danaee, S. Noori, Int. J. Hydrogen Energy 38 (2011) 4466–4473.
- [24] Z. Shan, Y. Liu, Z. Chen, G. Warrender, J. Tian, Int. J. Hydrogen Energy 33 (2008) 28–33.
- [25] M. Raney, US Patent No. 1,628,190, 1927.
- [26] S. Rondot, J. Cazaux, O. Aaboubi, J.P. Chopart, A. Olivier, Science 263 (1994) 1739–1741.
- [27] N. Ibl, Chem. Ing. Tech. 33 (1961) 69.
- [28] S. Trasatti, O.A. Petrii, Pure Appl. Chem. 63 (1991) 711–734.
- [29] J. Perez, H.M. Villalba, E.R. Gonzalez, J. Electroanal. Chem. 435 (1997) 179–187.
- [30] N.M. Markovic, B.N. Grgur, P.N. Ross, J. Phys. Chem. 101 (1997) 5405–5413.
- [31] C.K. Poh, Z. Tian, J. Gao, Z. Liu, J. Lin, Y.P. Feng, F. Su, J. Mater. Chem. 22 (2012) 13643–13652.
- [32] J.P. Meyers, in: S.J. Paddison, K.S. Promislow (Eds.), Device and Materials Modelling in PEM Fuel Cells, Springer, New York, 2009.
- [33] M.W. Kanan, D.G. Nocera, Science 321 (2008) 1072–1075.
- [34] A. Manabe, M. Kashiwase, T. Hashimoto, T. Hayashida, A. Kato, K. Hirao, I. Shimomura, I. Nagashima, Electrochim. Acta 100 (2013) 249–256.
- [35] E.B. Castro, C.A. Gervasi, Int. J. Hydrogen Energy 25 (2000) 1163–1170.
- [36] J. Chattopadhyay, R. Srivastava, P.K. Srivastava, J. Appl. Electrochem. 43 (2013) 279–287.
- [37] G. Li, H. Yu, X. Wang, S. Sun, Y. Li, Z. Shao, B. Yia, Phys. Chem. Chem. Phys. 15 (2013) 2858–2866.
- [38] Q. Yin, J.M. Tan, C. Besson, Y.V. Geletii, D.G. Musaev, A.E. Kuznetsov, Z. Luo, K.I. Hardcastle, C.L. Hill, Science 328 (2010) 342–345.
- [39] H.B. Hassan, Z.A. Hamid, Int. J. Hydrogen Energy 36 (2011) 5117–5127.
- [40] M.Z.F. Kamarudin, S.K. Kamarudin, M.S. Masdar, W.R.W. Daud, Int. J. Hydrogen Energy 38 (2013) 9438–9453.

- [41] C. Lamy, T. Jaubert, S. Baranton, C. Coutanceau, *J. Power Sources* 245 (2014) 927–936.
- [42] C. Désilet, A. Lasia, *Electrochim. Acta* 78 (2012) 286–293.
- [43] S. Rousseau, C. Coutanceau, C. Lamy, J.-M. Léger, *J. Power Sources* 158 (2006) 18–24.
- [44] A. Verma, S. Basu, *J. Power Sources* 168 (2007) 200–210.
- [45] E. Antolini, *J. Power Sources* 170 (2007) 1–12.
- [46] L. Han, H. Ju, Y. Xu, *Int. J. Hydrogen Energy* 37 (2012) 15156–15163.
- [47] O. Aaboubi, J. Amblard, J.-P. Chopart, A. Olivier, *J. Phys. Chem. B* 105 (2001) 7205–7210.
- [48] J.I.E. Gong, I. Zana, G. Zangari, *J. Mater. Sci. Lett.* 43 (2013) 279–287.
- [49] X. Xie, L. Gao, *Carbon* 45 (2007) 2365–2373.
- [50] W. Xiao, D. Wang, X.W. Lou, *J. Phys. Chem. C* 114 (2010) 1694–1700.
- [51] M.M.E. Duarte, A.S. Pilla, C.E. Mayer, *J. Appl. Electrochem.* 33 (2003) 387–392.